PNAS RESEARCH ARTICLE | BIOCHEMISTRY OPEN ACCESS

# Decoding in-cell respiratory enzyme dynamics by label-free in situ electrochemistry

Yoshihide Tokunou[a,b,1], Tomohiko Yamazaki[b,c], Takashi Fujikawa[b], and Akihiro Okamoto[a,b,d,e,f,1]

Affiliations are included on p. 11.

Edited by Michael Mirkin, Queens College, CUNY, Flushing, NY; received September 16, 2024; accepted February 7, 2025 by Editorial Board Member Lila M. Gierasch

**Deciphering metabolic enzyme catalysis in living cells remains a formidable challenge due to the limitations of in vivo assays, which focus on enzymes isolated from respiration. This study introduces an innovative whole-cell electrochemical assay to reveal the Michaelis–Menten landscape of respiratory enzymes amid complex molecular interactions. We controlled the microbial current generation's rate-limiting step, extracting in vivo kinetic parameters ($K_m$, $K_i$, and $k_{cat}$) for the periplasmic nitrite (NrfA) and fumarate (FccA) reductases. Notably, while NrfA kinetics mirrored those of its purified form, FccA exhibited unique kinetic behavior. Further exploration using a mutant strain lacking CymA, a periplasmic hub protein, revealed its crucial role in modulating FccA's kinetics, challenging the prevailing view that molecular crowding is the main cause of discrepancies between in vivo and in vitro enzyme kinetics. This platform offers a groundbreaking approach to studying cellular respiratory enzymatic kinetics, paving the way for future research in bioenergetics and medicine.**

interprotein interaction | Michaelis–Menten equation | enzymatic activity

Electron transfer in cellular respiration, vital to all living organisms, operates through a complex and synchronized network of molecular interactions. Traditional in vitro experiments have provided substantial insights into enzymatic reaction kinetics and protein structures, yet often fall short of replicating the intricate in vivo cellular milieu (1–3). This discrepancy has fueled ongoing debates in enzymology regarding the impact of physiological states and macromolecular crowding on enzymatic behavior (4, 5). Techniques to characterize in vivo enzymatic reaction kinetics have evolved, yet their application remains limited, often restricted to specific proteins, such as β-lactamase or alkaline phosphatase, and hindered by the complexities of cellular environments (6–9). A particularly challenging aspect is the elucidation of interprotein interactions within the respiratory electron transfer chain, which is pivotal for biological energy generation. Existing methods struggle to capture the enzyme catalysis in the presence of specific interprotein interactions without potentially altering enzymatic functions or associated electron and cation kinetics (6–9).

In the present study, we develop a groundbreaking label-free electrochemical approach to directly observe respiratory enzyme kinetics within intact bacteria. By enhancing microbial extracellular electron uptake from an extracellular electrode to an intracellular enzyme as the sole electron acceptor, we couple electrochemical current production with in vivo enzymatic catalysis. This approach circumvents the limitations of traditional bioelectrochemical techniques, which, despite their sensitivity and resolution, are impeded by the insulating properties of cellular membranes when applied to intracellular enzymes. Employing *Shewanella oneidensis* MR-1, renowned for its *c*-type cytochrome complexes (Cyts) on the outer membrane that facilitate direct electron transfer between intracellular enzymes and extracellular electrodes (10, 11), we developed a protocol for quantifying intracellular enzyme kinetics. Specifically, we utilized riboflavin to enhance electron transport through these cytochrome complexes to set the rate-limiting step as the intracellular enzymatic reaction (12, 13). By focusing on nitrite reductase (NrfA) and fumarate reductase (FccA), and examining their interactions with the electron donor hub protein CymA, we elucidate how these interactions influence their Michaelis–Menten kinetics. A series of antibiotics were used to quantify the contribution of these enzyme catalysis to the current production comparing to other biological processes. Furthermore, indirect electron transfer process via a soluble redox mediator was applied to monitor nitrate reductase activity in *Escherichia coli* using a high-throughput electrochemical system. Through this platform, we offer a first-of-its-kind insight into the in vivo kinetics of respiratory enzymes and their interprotein interactions, significantly advancing our methodology for understanding the complex symphony of cellular respiration.

## Significance

Understanding enzyme function in living organisms is vital for advancing biochemistry and therapeutic strategies. However, traditional in vivo enzyme assays have primarily focused on enzymes unrelated to complex respiration. This study introduces a pioneering approach to measure Michaelis–Menten kinetic parameters of respiratory enzymes within cells. By simply manipulating rate-limiting steps in microbial current generation via direct or indirect electron transfer mechanism, our real-time electrochemical assay revealed in vivo enzyme kinetics. Utilizing gene-knockout strains and inhibitors, we demonstrated that interprotein interactions shape enzyme activity, challenging the longstanding belief that molecular crowding accounts for differences between in vivo and in vitro kinetics. This breakthrough deepens our understanding of enzyme biochemistry and potentially transforms approaches in biomedical science.

The authors declare no competing interest.

This article is a PNAS Direct Submission. M.V.M. is a guest editor invited by the Editorial Board.



[1]To whom correspondence may be addressed. Email: tokunou.yoshihide.ga@u.tsukuba.ac.jp or okamoto.akihiro@nims.go.jp.

This article contains supporting information online at https://www.pnas.org/lookup/suppl/doi:10.1073/pnas.2418926122/-/DCSupplemental.

Published March 21, 2025.

## Results

**Shifting Rate-Limiting Step to Couple the Current Generation with Metabolic Enzymatic Reactions.** Cathodic current production in *S. oneidensis* MR-1 predominantly occurs when electrons are transferred from the electrode via the outer membrane Cyts and consumed by the periplasmic enzyme (12, 14) (Fig. 1*A*). To quantify the current production coupled with specific enzyme processes, it is essential to control the rate-limiting step within these multiple steps. More specifically, to fix the kinetics of the periplasmic enzymatic reaction as the rate-limiting step for cathodic current production, the rate of electron uptake via the Cyts has to be faster than the periplasmic enzymatic process (Fig. 1*A*).

To set the rate-limiting step as the periplasmic enzyme, we first focused on nitrite ($NO_2^-$) reduction, mediated by the NrfA protein, the sole nitrite reductase in the periplasmic space (15, 16). We added 10 μM riboflavin to enhance the rate of Cyts, as riboflavin is proven to significantly enhance electron transfer through outer membrane Cyts, particularly OmcA, by facilitating bound hydroquinone formation (12).

Utilizing a whole-cell electrochemical setup with MR-1 cells adsorbed on an indium tin-doped oxide (ITO) electrode within a three-electrode system under anaerobic conditions (see experimental) (17), we observed a stable microbe–electrode interface, with no significant change in the number of viable MR-1 cells over an hour in the presence of nitrite and 10 μM riboflavin (Fig. 1*B* and *SI Appendix*, Fig. S1), probably due to the short duration time and scarce generation of reactive oxygen species. The effect of riboflavin was validated in our electrochemical setup, where it markedly accelerated the cathodic current upon the introduction of 0.1 mM nitrite under a constant potential of −0.45 V vs. standard hydrogen electrode (SHE) (Fig. 1*C*). This effect was absent without riboflavin, where the cathodic current remained minimal. The slight cathodic current before nitrite addition, which was observed previously (12), can be explained by the consumption of substrate remaining from preculture. Additionally, this cathodic current was diminished in the absence of MR-1 cells or dead cells, and the addition of lactate as the electron source for MR-1 scarcely altered the current of MR-1 (*SI Appendix*, Fig. S2 and S3), indicating that the observed cathodic current is due to electron transport and consumption in MR-1 cells.

The linear relationship between the number of electrons delivered and nitrite consumed, with a correlation coefficient ($R^2$) of 0.99 (Fig. 1*E*), underscores the role of riboflavin in coupling cathodic current to the nitrite reduction reaction. Accordingly, the delivered electron and consumed nitrite ratio were compared, representing 5.92 ± 0.40 $e^-$/nitrite, which is stoichiometrically relevant with NrfA catalysis reducing nitrite to ammonia (6 $e^-$/1 nitrite) (Fig. 1*E* and *SI Appendix*, Fig. S4). Notably, the Δ*nrfA* mutant exhibited negligible current upon nitrite addition, affirming NrfA's attribution for the observed cathodic current increase (Fig. 1*C* and *SI Appendix*, Fig. S5).

Further, we conducted cyclic voltammetry (CV) on MR-1 cells to analyze the dependency of the cathodic current on the applied electrical potential. The CV revealed that the rate-limiting step shifted to nitrite reduction following riboflavin addition, with a clear cathodic current increase at an onset potential of −0.23 V (vs. SHE) in the presence of nitrite and riboflavin (Fig. 2*A*). This onset potential aligns with the enhanced electron transfer capabilities of cytochromes mediated by riboflavin (12). The concentration-dependent increase in cathodic current with nitrite in the presence of riboflavin (Fig. 2*A*), versus the absence of such dependency without riboflavin (Fig. 2*A*, *Inset*), illustrates that

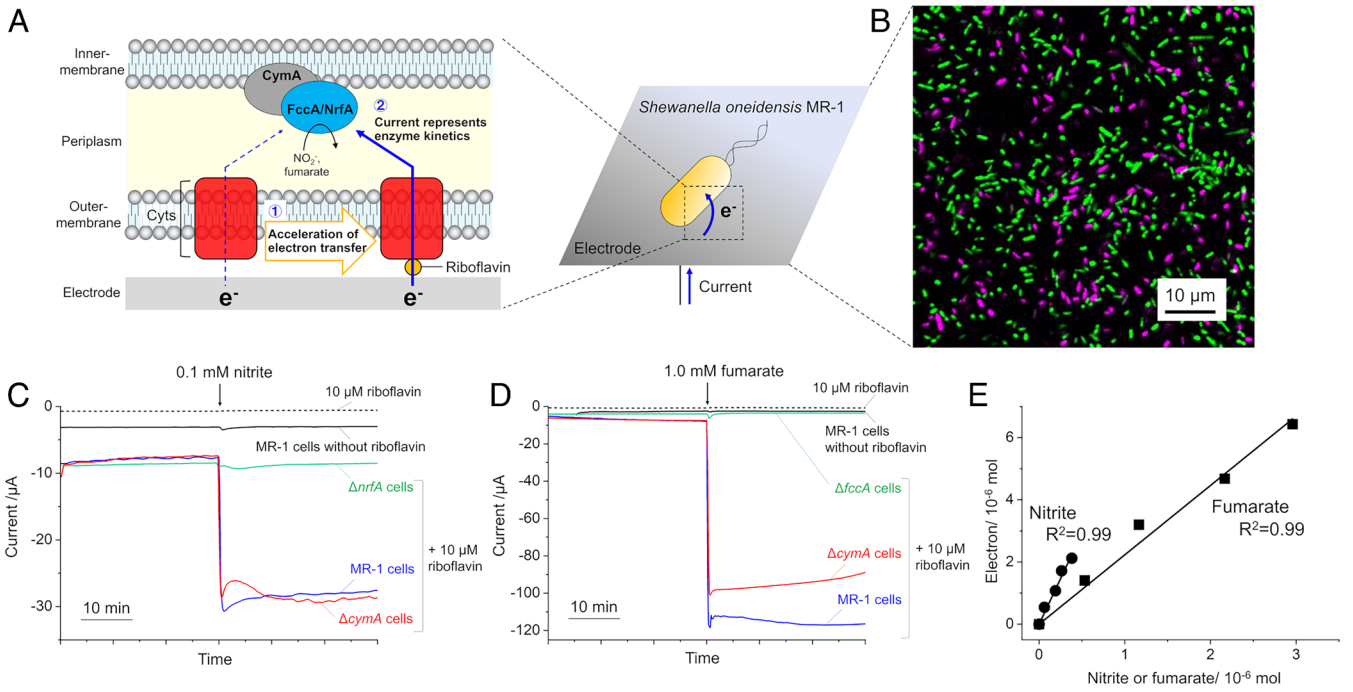


**Fig. 1.** The microbe–electrode system couples electrical current with nitrite and fumarate reduction. (*A*) Schematic illustration of electrochemical assay for respiratory enzyme kinetics. (*B*) A representative confocal microscopic image of *Shewanella oneidensis* MR-1 cells on ITO electrodes subjected to electrochemical assay, which is stained with SYTO 9 (green) and propidium iodide (magenta). (*C* and *D*) Representative time courses for cathodic current under potential application at −0.45 V (vs. SHE). Blue and black lines represent the cathodic current production from electrode-attached *S. oneidensis* MR-1 cells in the presence and absence of 10 μM riboflavin, respectively, and the dashed line is the current of 10 μM riboflavin without MR-1 cells. The red lines show the data of Δ*cymA* with 10 μM riboflavin. The green lines show the data of (*C*) Δ*nrfA* and (*D*) Δ*fccA* in the presence of 10 μM riboflavin. Arrows indicate the point at which (*C*) 0.1 mM nitrite and (*D*) 1.0 mM fumarate were added to each batch. The same tendency was reproduced in at least three separate experiments. (*E*) Representative plots of the number of electrons delivered to MR-1 cells against nitrite or fumarate consumption at an electrode potential of −0.45 V (vs. SHE). The baseline current was subtracted from the electron number. The squares of the correlation coefficients ($R^2$) include the point of origin.

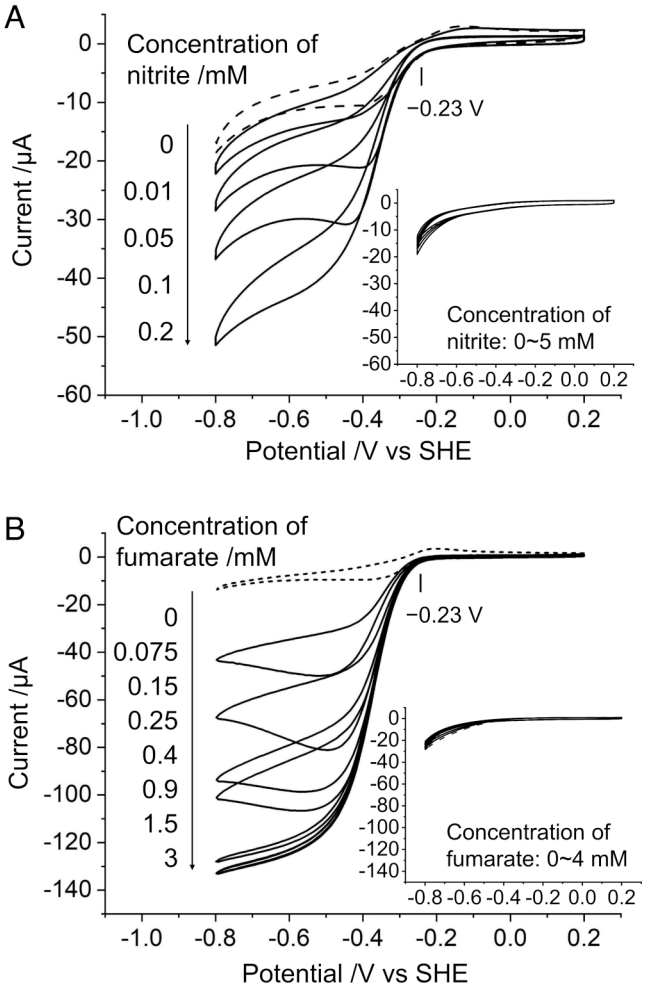


**Fig. 2.** Riboflavin shifts the rate-limiting step of current production from electron uptake to the enzymatic reaction. Cyclic voltammograms of *S. oneidensis* MR-1 cells with nitrite (*A*) and fumarate (*B*) in the presence of 10 μM riboflavin. The dashed lines represent the data without nitrite and fumarate. The data with 1.5 mM and 3.0 mM fumarate are overlapping. The scan rate is 10 $mVs^{-1}$. The same tendency was reproduced in at least three separate experiments. Inset: Data of *S. oneidensis* MR-1 cells without riboflavin.

nitrite reduction at NrfA limits the cathodic current in the presence of riboflavin.

Similarly, the addition of 1.0 mM fumarate in the presence of 10 μM riboflavin resulted in an immediate cathodic current increase of about −115 μA, a response absent in the Δ*fccA* mutant, indicating FccA's role in fumarate reduction (Fig. 1*D* and *SI Appendix*, Fig. S5). The stoichiometric correlation between cathodic current and fumarate consumption (2.06 ± 0.33 $e^-$/fumarate) closely matches the theoretical reduction ratio (Fig. 1*E* and *SI Appendix*, Fig. S4). Furthermore, the cathodic current in CV also increased with fumarate concentration in the presence of riboflavin (Fig. 2*B*), demonstrating the coupling of microbial current production with intracellular enzyme catalysis in the presence of riboflavin. This coupling was not observed without riboflavin (Fig. 2*B*, *Inset*), highlighting the essential role of riboflavin in facilitating intracellular enzymatic reactions and their corresponding electrochemical signatures.

To confirm that the electrical output is solely derived from the enzyme catalysis with scarce interference from other intracellular processes, the microbial cathodic current response against an ATPase inhibitor, N,N-dicyclohexylcarbodiimide, and a proton ionophore, carbonyl cyanide 3-chlorophenylhydrazone were monitored in the presence of 5.0 mM fumarate and 10 μM riboflavin. Both additives scarcely altered the current profile (Fig. 3 *A* and *B* and *SI Appendix*, Fig. S6), strongly suggesting that the current is connected to the intracellular enzyme catalysis without being linked with proton translocation across the inner membrane. We also tested five types of antibiotics with different mechanisms of action such as imipenem (β-lactam antibiotics), ciprofloxacin (new quinolone antibiotics), amikacin (aminoglycoside antibiotics), chloramphenicol, and polymyxin B (polypeptide antibiotics). In the case of imipenem, ciprofloxacin, amikacin, and chloramphenicol, over 90% of the cathodic current remained at even higher concentrations than the minimum inhibitory concentration (MIC) (Fig. 3 *C*–*F* and *SI Appendix*, Fig. S6), suggesting that the electrical output is scarcely interfered with by other intracellular processes linked with cell wall synthesis, DNA synthesis, protein synthesis, and cell growth. In contrast, polymyxin B and ethanol largely diminished the cathodic current (Fig. 3*G* and *SI Appendix*, Figs. S6 and S7). Because both polymyxin B and ethanol disrupt the outer membrane sustaining Cyts that electrically connect the electrode and the periplasmic enzyme, these data suggest that the other biological process than enzyme and electron uptake does not impact the cathodic current, highlighting the versatility of our method to applying to other enzymes. Although ethanol potentially impacts cell activity through other mechanisms, such as interference with ATP production (18), the minimal effect observed with the ATPase inhibitor and proton ionophore suggests that the primary cause of the current decrease is likely the disruption of the outer membrane.

**Michaelis–Menten Analysis of Intracellular NrfA and FccA Catalysis.** To characterize the kinetic properties of intracellular NrfA using whole-cell electrochemistry, we analyzed the cathodic current at various concentrations as reported for purified NrfA with the Michaelis–Menten equation (19). The cathodic current in the presence of riboflavin gradually decreased at higher concentrations than 0.4 mM (*SI Appendix*, Fig. S8), characteristic of purified NrfA protein exhibiting substrate inhibition at high nitrite concentration (19). This trend is evident by plotting the nitrite reduction kinetics against the concentration of nitrite (Fig. 4*A*). Nitrite reduction kinetics is calculated from the limiting current (the cathodic current at −0.80 V vs. SHE in CV following subtraction by the cathodic currents in the absence of nitrite) and the amount of NrfA present in the MR-1 cells attached on each ITO electrode quantified by liquid chromatography-mass spectrometry (LC-MS) analysis [4.63 ± 0.55 pmol (*SI Appendix*, Fig. S9)].

$$v = \frac{V_{max}[S]}{K_m + [S](1 + [S]/K_i)}, \quad [1]$$

Eq. **1** is a Michaelis–Menten model in which a second substrate molecule binds to inhibit the enzyme that applies to purified NrfA protein (19). $K_m$ and $K_i$ are Michaelis constant and inhibition constant, and $V_{max}$ and [S] are maximum turnover rate and nitrite concentration, respectively. The plots of nitrite reduction kinetics were fitted with this model (Fig. 4*A*), demonstrating that intracellular NrfA shows reaction kinetics following the Michaelis–Menten equation as with the purified one. $K_m$, $K_i$, and $V_{max}$ were determined to be 63.0 ± 13.7 μM, 19.7 ± 3.2 mM, and 94.5 ± 16.8 pmol $s^{-1}$, respectively (Figs. 4*B* and 3*C*). $k_{cat}$ (turnover number) of NrfA was calculated to be 20.4 ± 4.37 $s^{-1}$ (Table 1 and *SI Appendix*, Fig. S9). The $K_m$ and $K_i$ of NrfA in an intact cell were almost identical to those of purified NrfA protein immobilized on electrodes: 54 ± 12 μM for $K_m$ and 18 ± 4 mM for $K_i$ (Fig. 4 *B* and *C*) (19).

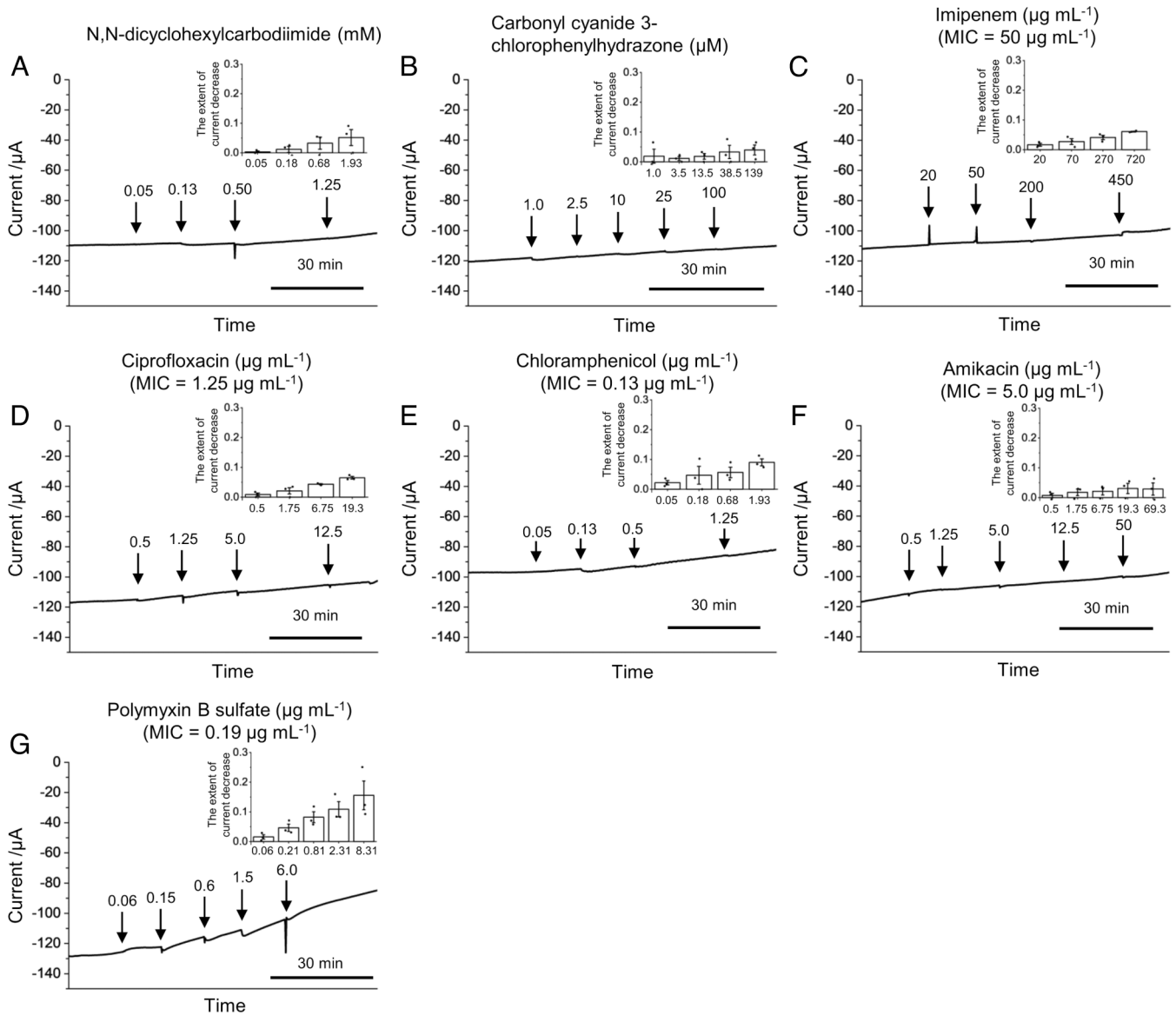


**Fig. 3.** (*A-G*) The impact of antibiotics and inhibitors on the electrical current in the microbe–electrode system. Representative time courses for cathodic current from electrode-attached *S. oneidensis* MR-1 cells under potential application at −0.45 V (vs SHE) with 10 μM riboflavin and 5.0 mM fumarate. Each antibiotic or inhibitor was added at the times indicated by the arrows. The types and concentrations of antibiotics/inhibitors are noted. The minimum inhibitory concentration (MIC) for each antibiotic, determined by the growth in the defined medium (DM) containing 10 mM lactate under aerobic conditions, is also indicated. *Inset*: The relative cathodic current decreases at 10 min after the addition of antibiotics or inhibitors. The error bars represent the mean ± SEM obtained from three separate experiments.

In contrast, the kinetics of FccA differed significantly from analogous purified proteins. The plot of fumarate reduction kinetics against fumarate concentration showed nonproportional relationships following a Michaelis–Menten curve (Fig. 4*D*). Hanes–Woolf plots were made to quantify $K_m$ of intracellular FccA (Fig. 4*E*).

$$v = \frac{V_{max}[S]}{K_m + [S]}(\text{Michaelis} - \text{Mentenequation}), \quad [2]$$

$$\frac{[S]}{v} = \frac{[S]}{V_{max}} + \frac{K_m}{V_{max}}(\text{Hanes} - \text{Woolfplots}), \quad [3]$$

$K_m$ and $V_{max}$ were revealed to be 161 ± 23.6 μM and 751 ± 72.0 pmol $s^{-1}$ via the linear regression of Hanes–Woolf plots (Fig. 4*F*). $k_{cat}$ of FccA was 182 ± 37.4 $s^{-1}$ (Table 1 and *SI Appendix*, Fig. S10). The $K_m$ value of purified FccA protein has been reported to be below 50 μM (22) and analogous fumarate reductase from *Shewanella frigidimarina* [with 59% amino acid sequence identity (23)] showed $K_m$ of 21 μM or 6 μM (20, 21). These values are significantly lower than the $K_m$ of FccA in the cells (Fig. 4*F*).

The potential discrepancy between the bulk and the periplasmic fumarate concentration was investigated by increasing the membrane permeability with polymyxin B. This substance creates pores in the cell's outer membrane, allowing polypeptides to pass through (24). In our study, MR-1 cells supplemented with riboflavin were treated with 6.0 μg $mL^{-1}$ polymyxin B, a dose known to increase their membrane permeability (25). CV showed that the cathodic current response to fumarate was similar, regardless of polymyxin B treatment until 0.9 mM (*SI Appendix*, Fig. S11). This is consistent with conventional studies that bacterial outer membranes are typically permeable against most carbohydrates, scarcely making the substrate concentration gradient a limiting

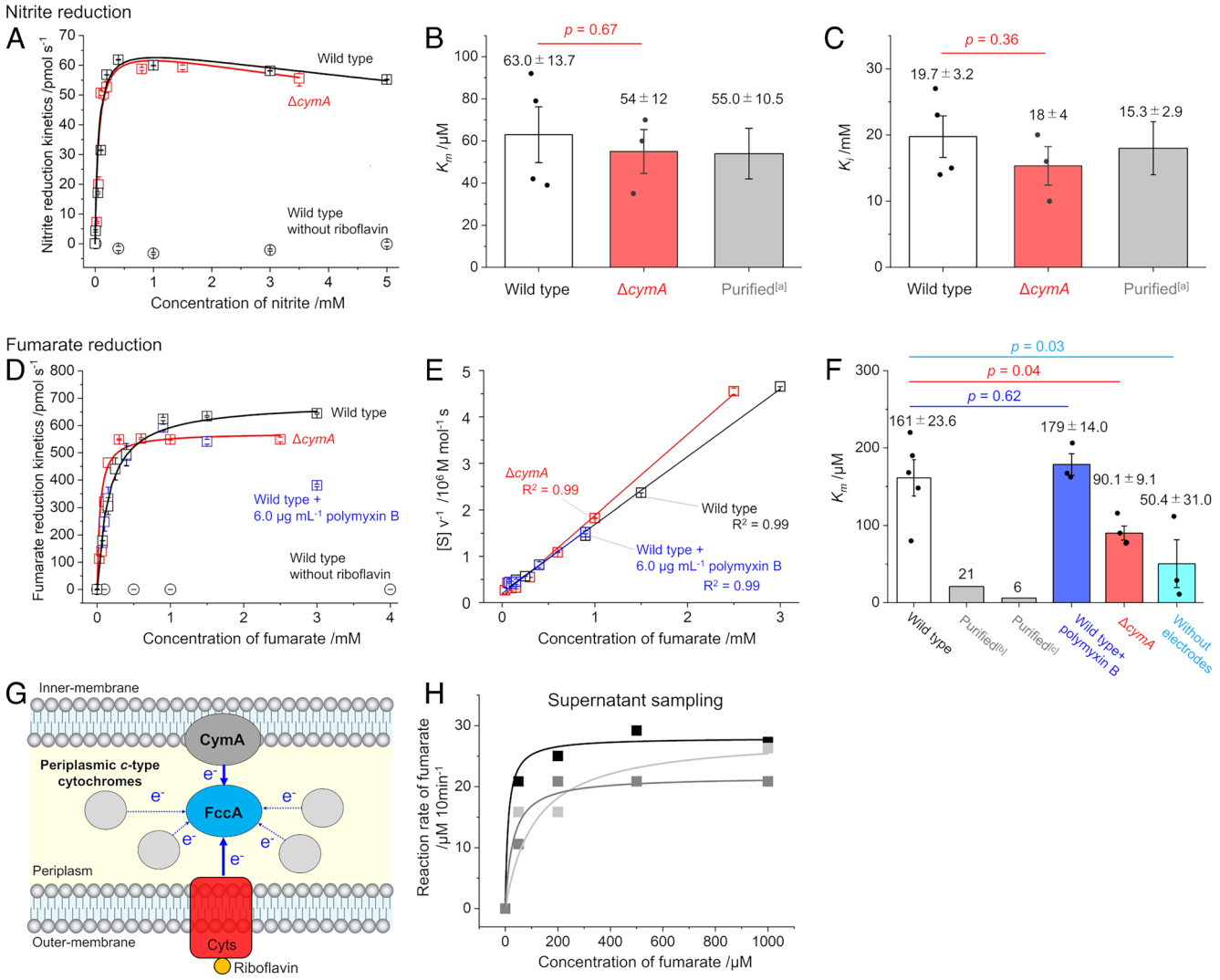


**Fig. 4.** Michaelis–Menten analysis for electrochemical nitrite and fumarate reduction in intact cells. (*A*) Representative plots of nitrite reduction rate against the concentration of nitrite. The black square and black circle plots represent the data in the presence and absence of 10 μM riboflavin, respectively. Red plots are the data for Δ*cymA* cells with 10 μM riboflavin. The error bars represent the mean ± SEM obtained from three times CV scans using the same reactor. The same tendency was reproduced in at least three separate experiments. The solid line represents a fitting line based on the Michaelis–Menten equation. $K_m$ (*B*) and $K_i$ (*C*) of nitrite reduction in MR-1 cells. White and red bars represent the data for wild type and Δ*cymA*, respectively. Gray bars represent the data for purified homologous proteins [(*A*): ref. 19]. Numerical data are indicated above the bars. The error bars represent the mean ± SEM obtained from at least three separate experiments. Statistical significance is determined by *P*-values from two-sided Student's *t* test compared to the wild type. (*D*) Representative plots of reaction kinetics against the concentration of fumarate. The black square and black circle plots represent the data in the presence and absence of 10 μM riboflavin, respectively. Red plots are the data for Δ*cymA* cells with 10 μM riboflavin. Blue plots are the data with 6.0 mg $L^{-1}$ polymyxin B and 10 μM riboflavin. The error bars represent the mean ± SEM obtained from three times CV scans using the same reactor. The same tendency was reproduced in at least three separate experiments. (*E*) Representative Hanes–Woolf plots for fumarate reduction kinetics in the absence (black plots) and presence (blue plots) of 6.0 μg $mL^{-1}$ polymyxin B. Red plots represent the data of Δ*cymA* cells. The error bars represent the mean ± SEM obtained from three times CV scans using the same reactor. The same tendency was reproduced in at least three separate experiments. (*F*) $K_m$ of fumarate reduction reaction in MR-1 cells. Blue bars represent the data for wild type in the presence of 6.0 mg $L^{-1}$ polymyxin B and light blue bar represents $K_m$ of fumarate reduction in sealed bottles without electrodes. Gray bars represent the data for purified proteins [(*B*): ref. 20, and (*C*): ref. 21]. (*G*) An illustration of FccA accepting electrons from the periplasmic proteins in MR-1 cells. (*H*) Plots of fumarate consumption rate by MR-1 cells against fumarate concentration in sealed bottles without electrodes from three independent experiments.

factor, unlike metabolites (26). The antibiotic effect of polymyxin B potentially disturbing the electron transfer pathways may explain the current reduction at the higher concentrations (Fig. 3*G*). Analysis of the data, including linear regression of Hanes–Woolf plots, yielded a $K_m$ of 179 ± 14.0 μM (Fig. 4 *E* and *F*), suggesting that differences in enzyme kinetics between in vivo and purified conditions are not primarily due to the periplasmic space effects on localized substrate concentration. This indicates that factors other than the periplasmic concentration contribute to the kinetic discrepancies observed between purified enzymes and those functioning within cellular environments.

**The Impact of Interprotein Interaction on $K_m$ in Intact Cells.** Despite previous reports suggesting crowding effects on the periplasmic enzyme reactions (27), our observations indicate that such effects are minimal for FccA. This inference is supported by the consistent kinetics between NrfA in its purified form and within the cell, and the action of polymyxin B, which also releases polynucleotides from the cell inside, suggesting a negligible impact of crowding on FccA activity. Crucially, FccA is known for its specific and strong interaction with CymA (14, 28, 29), a distinct factor with the nonspecific nature of crowding effects. To elucidate the influence of interprotein interactions

**Table 1. Turnover number ($k_{cat}$) of NrfA and FccA in MR-1 cells on ITO electrodes**

| | $V_{max}$ / pmol $s^{-1}$ | The amount of proteins on an ITO electrode /pmol | $k_{cat}$ /$s^{-1}$ |
|---|---|---|---|
| NrfA in wild type | 94.5 ± 16.8 | 4.63 ± 0.55 | 20.4 ± 4.37 |
| NrfA in Δ*cymA* | 97.8 ± 13.6 | 6.01 ± 0.35 | 16.3 ± 2.46 |
| Purified NrfA | – | – | 7 ± 2 |
| FccA in wild-type | 751 ± 72.0 | 4.12 ± 0.75 | 182 ± 37.4 |
| FccA in Δ*cymA* | 484 ± 128 | 5.00 ± 0.66 | 96.9 ± 28.6 |
| Purified FccA | – | – | 250 |

The $k_{cat}$ of purified NrfA and FccA were cited from refs. 19 and 20 respectively.

on in vivo enzyme kinetics, we investigated the Δ*cymA* mutant strain, which lacks the CymA protein, a key component in the electron transfer chain. Upon the addition of nitrite, the Δ*cymA* mutant strain exhibited an increase in cathodic current similar to that observed in the wild type strain, indicating that the electron transfer mechanism compensates for the absence of CymA in nitrite reduction (Fig. 1*C*). However, upon introducing 1.0 mM fumarate, the cathodic current observed in the Δ*cymA* strain was notably 10 to 20% lower than that in the wild type (Fig. 1*D*), despite similar fumarate reductase FccA levels in both strains (Table 1). This discrepancy underscores a specific limitation in the fumarate reduction pathway attributable to the absence of CymA.

Further analysis revealed a concentration-dependent effect of nitrite or fumarate on the cathodic limiting current, confirming FccA and NrfA as limiting factors in their respective reduction reactions (*SI Appendix*, Fig. S12). While the CymA protein is essential electron donor for FccA under lactate feeding condition in MR-1 (14, 28, 29), these data strongly suggest that FccA and NrfA appear to receive electrons more readily from the outer-membrane cytochrome complex MtrCAB or the periplasmic *c*-type cytochromes such as STC and CcpA, bypassing the need for direct interaction with CymA during the reduction of fumarate and nitrite in the absence of CymA (Fig. 4*G*) (30).

Kinetic analysis of the cathodic response to fumarate addition, following Michaelis–Menten kinetics, revealed a significant alteration in the catalytic efficiency of FccA in the Δ*cymA* strain (Fig. 4*D*), with a $K_m$ value approximately half that of the wild type (Fig. 4*F* and *SI Appendix*, Fig. S12). The observed changes in the $k_{cat}$ for fumarate reduction, which decreased by about 47% in the Δ*cymA* strain (Table 1), further emphasize the critical role of the FccA–CymA complex in modulating fumarate reduction kinetics. Conversely, the kinetic parameters, $K_m$ and $K_i$, for NrfA in the Δ*cymA* strain remained nearly identical to those of the wild type (Fig. 4 *B* and *C*), and the $k_{cat}$ for nitrite reduction in the Δ*cymA* strain was comparable to that of the wild type (Table 1 and *SI Appendix*, Fig. S10), reinforcing the differential impact of CymA on the kinetics of FccA and NrfA. Taken together, these results demonstrate that the formation of the FccA–CymA complex has a critical role in regulating fumarate reduction kinetics.

Such a clear indication of FccA activity and FccA–CymA interaction was not visible in conventional metabolite analysis. By measuring fumarate consumption under anaerobic conditions with lactate as the electron donor, without the use of electrodes, we observed significant fumarate reduction in wild type cells (*SI Appendix*, Fig. S13). In contrast, the Δ*cymA* mutant exhibited minimal fumarate reduction over 90 min, whereas the wild type strain nearly exhausted its fumarate supply (*SI Appendix*, Fig. S13). This stark difference underscores the critical role of CymA as an essential electron donor for FccA activity when lactate serves as the electron source (31). Furthermore, the estimated $K_m$ value for fumarate reduction in wild type cells (50.4 ± 31.0 μM) was distinct from that determined electrochemically (Fig. 4 *F* and *H*). This discrepancy likely stems from the inability of traditional metabolite analysis to precisely identify rate-limiting steps among sequential multiple metabolic reactions, resulting in a less detailed understanding of enzyme kinetics. These findings highlight the superior precision and specificity of electrochemical assays in elucidating intracellular enzyme kinetics.

**Investigating the Impact of CymA on the Binding Affinity of FccA–Fumarate in Intact Cells.** To further explore the mechanism for CymA to impact the FccA kinetics, we examined the fumarate binding affinity. $K_m$ decreases when $k_{cat}$ decreases or the binding affinity between enzyme and substrate increases (Fig. 5*A*). Because the gene deletion of *cymA* decreased $k_{cat}$ associated with the decrease of $K_m$, it is unclear whether the binding affinity of FccA with fumarate is altered by the interaction with CymA. To test this point, we measured the $K_i$ for the fumarate reduction using mesaconic acid as a competitive inhibitor (20). Because mesaconic acid binds with FccA to block fumarate reduction, $K_i$ excludes the information about the turnover rate and reflects the affinity of fumarate to the binding site in FccA. We added a variety of concentrations of mesaconic acid to MR-1 cells on the electrode in the presence of 5.0 mM fumarate and 10 μM riboflavin. The addition of mesaconic acid decreased the cathodic limiting current as shown in the CV in *SI Appendix*, Fig. S14*A*. To quantify the inhibition effect, $K_i$ was calculated following the Michaelis–Menten equation.

$$v = \frac{V_{max}[S]}{K_m(1 + [I]/K_i) + [S]}. \quad [4]$$

where [I] and $K_i$ represent the concentration of mesaconic acid and constant for competitive inhibition, respectively. Eq. **4** provides Eq. **5** as follows.

$$\frac{V_{max}}{v} = \frac{K_m}{K_i[S]}[I] + \frac{K_m + [S]}{[S]}. \quad [5]$$

According to Eq. **5**, $V_{max}/v$ linearly increases with [I], providing $K_m/K_i[S]$ as a slope. Consistently, the plots of $V_{max}/v$ against [I] showed a linear relationship with the squares of the correlation coefficient ($R^2$) of 0.97 (Fig. 5*B* and *SI Appendix*, Fig. S14), further supporting that mesaconic acid inhibits intracellular FccA. From the slope, $K_i$ was revealed to be 583 ± 147 μM (Fig. 5*C*). This $K_i$ value is slightly larger than that of Δ*cymA*, 419 ± 150 μM, but Student's *t* test confirmed no significant difference, while the distinct $K_i$ in the purified enzyme suggests the flexible fumarate binding affinity (Fig. 5*C*). These data indicate that FccA–CymA interaction likely affects $k_{cat}$ rather than the binding affinity. Purified CymA binds with FccA near a heme that does not directly contact the active site to convert fumarate into succinate (30, 32). Thus, it is reasonable that the FccA–CymA interaction scarcely affects the binding affinity.

**Application of the electrochemical assay to *E. coli* in 96-well three-electrode systems.** To evaluate the general applicability of our in vivo enzyme kinetic analysis, two significant challenges need to be addressed. First, performing Michaelis–Menten analyses requires electrochemical measurements across multiple concentration conditions using both wild type and knockout strains. Ensuring reproducibility necessitates a substantial

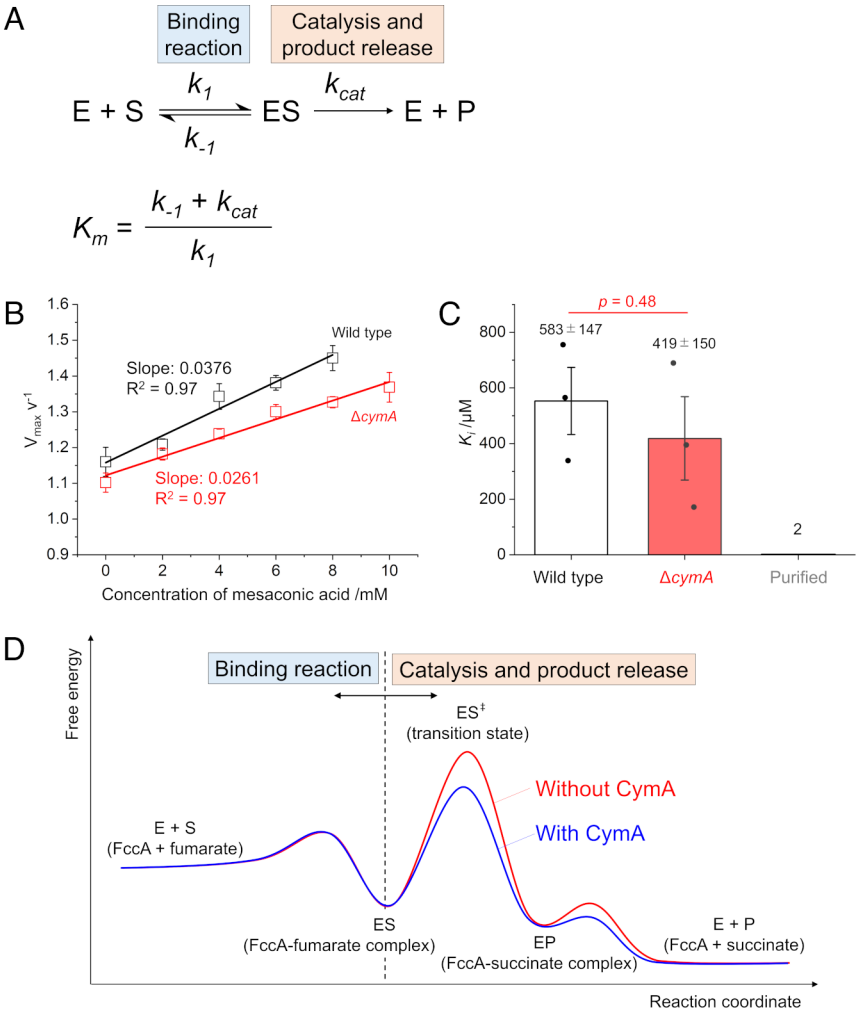


**Fig. 5.** The impact of CymA on fumarate reduction kinetics. (*A*) Michaelis–Menten reaction scheme and the definition of $K_m$. E, enzyme; S, substrate; ES, complex of enzyme–substrate; P, product; *k*, rate constant. (*B*) Representative plots of $V_{max}/v$ against the concentration of mesaconic acid for wild type (black) and Δ*cymA* (red). v was obtained from the cathodic limiting current and the amount of FccA in the MR-1 cells attached to each ITO electrode. The error bars represent the mean ± SEM obtained from three times CV scans using the same reactor. The same tendency was reproduced in three separate experiments. (*C*) $K_i$ for fumarate reduction. The white and red bars represent the data for wild type and Δ*cymA*, respectively, measured by whole-cell electrochemical assay, and the gray bar represents the data for purified protein (ref. 20). Numerical data are indicated above the bars. The error bars represent the mean ± SEM obtained from three separate experiments. Statistical significance is determined by *P*-values from two-sided Student's *t* test compared to wild type. (*D*) An illustration of FccA–fumarate reaction coordinates in the presence and absence of CymA.

number of electrochemical experiments. Second, the scope of target enzymes may be restricted to host microorganisms such as *Shewanella*, which utilize direct electron transfer mechanisms via outer membrane Cyts. However, indirect electron transfer using soluble redox molecules has been well documented (33), suggesting that intracellular enzyme activity can also be observed through such mechanisms (Fig. 6*A*). To test this hypothesis, we used *E. coli* strains lacking outer membrane cytochromes, along with safranin, a molecule characterized by high solubility and negative redox potential, to determine whether Michaelis–Menten plots could be obtained.

To address the labor-intensive nature of these experiments, we utilized a high-throughput electrochemical measurement system with proven performance in indirect electron transfer (34, 35). This system incorporates a 96-well plate with three-electrode configurations printed at the bottom of each well (Fig. 6*B*), enabling simultaneous electrochemical measurements across all wells. Although previously only constant potential measurements had been reported using this system (34, 35), we modified the control setup to allow potential sweeps. Using this enhanced system, we conducted CV with safranin solutions, confirming that all wells successfully performed CVs (Fig. 6*C*) and exhibited redox potentials consistent with established electrochemical systems (*SI Appendix*, Fig. S15) (36). This represents a system capable of 96 CV measurements parallelly, significantly reducing the experimental workload and enhancing reproducibility across varying conditions.

Next, using this system, we performed Michaelis–Menten analyses of the periplasmic nitrate reductase enzyme (NarG) in wild type and a knockout *E. coli* strain (Δ*narG*) (Fig. 6*D*). When CVs were conducted with 1.0 mM safranin, wild type cells exhibited a cathodic current dependent on nitrate concentration (Fig. 6*E*), a response that was diminished in Δ*narG* strains (Fig. 6*F*) and absent in control conditions lacking safranin (*SI Appendix*, Fig. S16). These findings suggest that nitrate reduction by NarG limits the cathodic current in the presence of safranin. The cathodic current followed a Michaelis–Menten curve with an $R^2$ of 0.759, yielding a $K_m$ value of 194 μM (Fig. 6*G*), comparable to the reported $K_m$ for NarG from *Salmonella enterica* (123 ± 14 μM) (37). In contrast, the cathodic current for the Δ*narG* strain resulted in an $R^2$ of 0.005, indicating the absence of nitrate reduction activity. These results strongly suggest that the $K_m$ derived using the 96-well electrochemical system reflects NarG catalysis

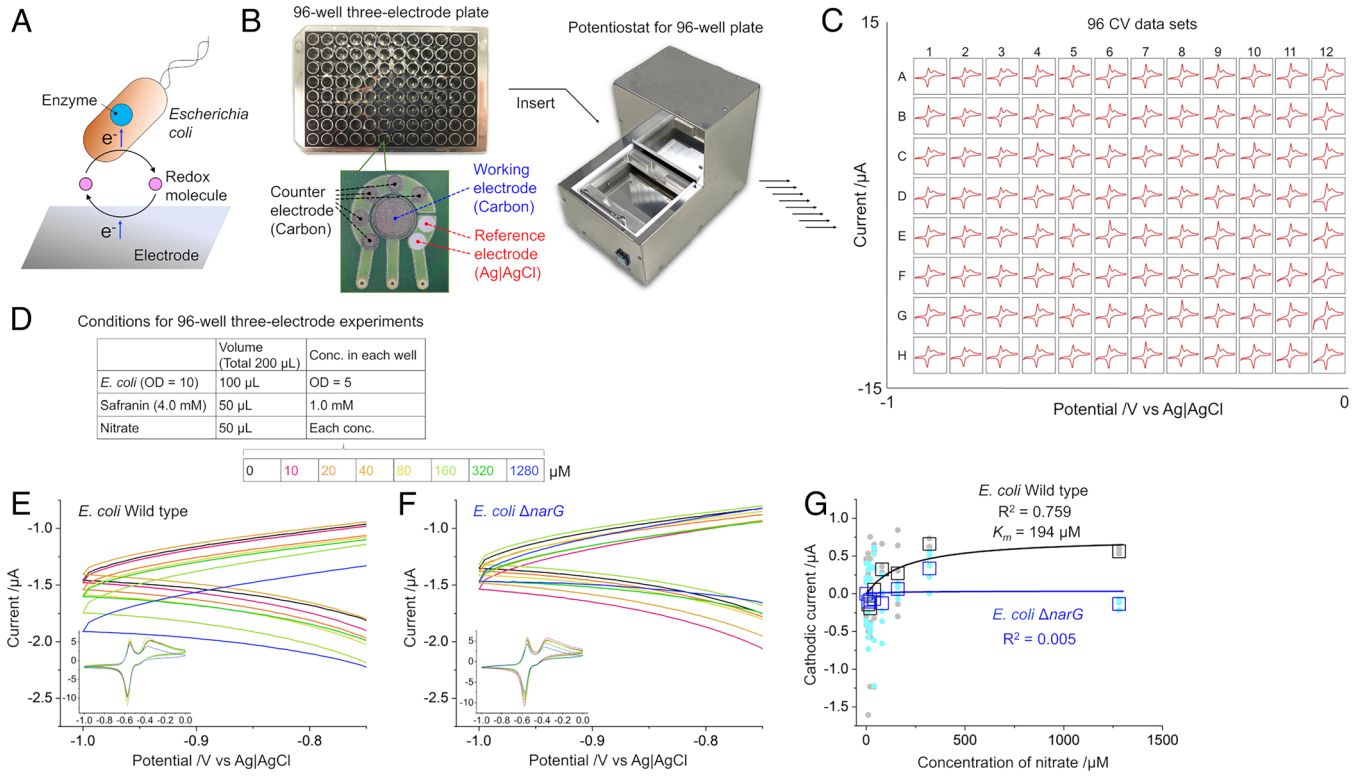


**Fig. 6.** High-throughput electrochemical system for in vivo enzyme assays in *Escherichia coli*. (*A*) Schematic representation of indirect electron transfer via a soluble redox mediator in *E. coli* lacking outer membrane cytochromes (Cyts). (*B*) Photos of the 96-well three-electrode electrochemical plate and device. Each well is equipped with screen-printed electrodes: a carbon working electrode, a carbon counterelectrode, and an Ag/AgCl reference electrode. (*C*) An example dataset showing 96 cyclic voltammograms (CVs) parallelly obtained using the system. (*D*) Conditions for the electrochemical assay on *E. coli*. (*E*) Representative CVs for wild type *E. coli* in the presence of 1.0 mM safranin and varying nitrate concentrations. (*F*) Representative CVs for *ΔnarG* mutant *E. coli* under the same conditions. Scan rate: 5 mV $s^{-1}$. (*G*) Cathodic current at −1.0 V vs. Ag/AgCl plotted against the nitrate concentrations. Gray (wild type) and light blue (*ΔnarG*) plots represent each cathodic current from each well normalized by the current without *E. coli* cells, where large cathodic currents are represented to be positive. Black and blue square plots represent the average data at each nitrate concentration. Black and blue lines represent the fitting Michaelis–Menten curves determined by the least-squares method. The $R^2$ was 0.759 for wild type and 0.005 for *ΔnarG*. At least three independent CVs were obtained for each condition.

in *E. coli*. Although the cathodic current values were not particularly high and the resulting Michaelis–Menten plots were not exceptionally well-defined, these findings demonstrate that in vivo enzyme analysis is feasible even with indirect electron transfer. By leveraging the high-throughput potential-sweeping system to efficiently screen for electron mediators that enhance catalytic current measurements, this methodology could achieve even greater accuracy in intracellular enzyme analyses.

## Discussion

The exploration of electron transfer in respiration, a cornerstone of living systems, has historically been studied through the extraction and separation of partner enzymes (38). This approach has significantly contributed to our understanding of biochemical reaction mechanisms, yet the analysis of respiratory enzymatic kinetics, especially within living cells, has remained elusive due to methodological limitations, including the absence of systems capable of monitoring electron flux without the need for labeling.

In microbial electrochemistry, studying bacteria that can exchange electrons with electrodes—acting as living electrochemical catalysts—has been ongoing for over two decades, primarily within the energy and environmental sectors (39, 40). These studies have largely focused on the mechanisms of interfacial electron transfer and the elucidation of respiratory pathways, with less attention given to the kinetics of intracellular enzymes. Our research pivots this focus toward in vivo monitoring of the periplasmic enzyme kinetics in the model electrogenic bacterium, *S. oneidensis* MR-1. By facilitating electron uptake from a negatively poised electrode through Cyts, we redirected the rate-limiting step from interfacial electron uptake to the reduction of nitrite or fumarate. This approach allowed us to determine in vivo kinetic parameters, including $K_m$, $K_i$, and $k_{cat}$, for the periplasmic enzymes NrfA and FccA, revealing similar and distinct kinetics, respectively, between the purified and cellular states of these enzymes.

Our findings highlight the impact of specific interprotein interactions on enzyme kinetics, particularly demonstrated by the significant changes in $K_m$ and $k_{cat}$ for FccA, but not NrfA, following the deletion of the *cymA* gene. Because the gene deletion scarcely influenced the $K_i$ of FccA with a competitive inhibitor, the interaction between FccA and CymA likely affects $k_{cat}$ rather than the binding affinity. Given $k_{cat}$ represents the enzymatic turnover number linked with postprocesses of enzyme–substrate binding, the FccA–CymA interaction would primarily accelerate the postprocesses of FccA–fumarate binding, such as product release or conformational change (Fig. 5 *A* and *D*), of which dynamics is difficult to monitor in purified protein systems (29). This highlights that the transient complex formation of proteins in respiratory electron transfer is pivotal in defining enzymatic catalysis within the cellular context.

Furthermore, our study challenges the conventional belief that macromolecular crowding is the primary cause for the difference between in vivo and in vitro enzyme kinetics (4, 5). By modulating the macromolecular concentration within the periplasmic space

using polymyxin B, which allows for the permeation of both fumarate and polypeptides across the outer membrane (24), we observed that changes in macromolecular crowding did not notably affect enzyme kinetics. This was in stark contrast to the effects seen with the deletion of the *cymA* gene, which led to a significant decrease in the $K_m$ values for FccA, suggesting that the deletion of *cymA* rather not impact macromolecular crowding but significantly alters enzyme kinetics through changes in interprotein interactions. The relatively minor abundance of CymA compared to the total biomolecular content within cells (41), and its capacity to interact flexibly with various proteins in the periplasm (42) further support the conclusion that interprotein interactions exert a more substantial influence on the kinetics of FccA than previously recognized effects of macromolecular crowding.

Whereas the $K_i$ of FccA in wild type was almost identical to that in Δ*cymA*, but was largely different from those for purified fumarate reductase from *S. frigidimarina* (Fig. 5*B*). This reveals that interactions with proteins other than CymA can modulate $K_i$, indicating a complex network of protein interactions affecting FccA's activity. The dual functionality of FccA further illustrates this complexity within cells, which, in association with CymA, may serve not only in its canonical role in fumarate reduction but also as an electron storage mechanism within the periplasmic space (*SI Appendix*, Fig. S18) (43). These dual roles facilitate the temporary storage of respiratory electrons, contributing to forming a proton motive force and transmitting electrons to other enzymes, thereby terminating the reduction reactions of various substrates (43). This could indicate the importance of specific interprotein interactions in shaping the functional landscape of enzymes within the complex cellular environment.

Previous methods for measuring enzymes within cells required the enzymes to function independently to obtain kinetic parameters, restricting the breadth of measurable targets (6–9). Our study has successfully tracked enzyme reactions within the complex network of the respiratory chain. By leveraging riboflavin to enhance electron transfer through Cyts, we were able to set the enzymatic reaction as the rate-limiting step. Riboflavin's specificity and high binding affinity to Cyts significantly accelerate electron transfer, enabling precise quantification of reaction kinetics for respiratory enzymes that receive electrons from Cyts. Ion chromatography measurements of fumarate and nitrite consumption showed a conversion efficiency of nearly 100% (Fig. 1*E*). This indicates that the cathodic current directly correlates with intracellular reduction reactions. The core principle of our assay—that the electrode acts exclusively as the electron donor and a specific enzyme as the sole electron acceptor—ensures high electron-substrate conversion efficiency and limits cathodic current only to the intended reactions.

Despite complex electron transfer pathways, our method directs electrons to the target enzyme. While other redox-active enzymes or proteins may initially consume some electrons, these are negligible in our system since one electron acceptor substrate is provided, and competing enzymes do not recycle electrons catalytically. The electron flow toward the primary substrate vastly outweighs any diversion to nontarget enzymes ($10^{-6}$ mol $s^{-1}$ scale for primary substrate versus $10^{-9}$ mol $s^{-1}$ for nontargets, *SI Appendix*, Fig. S17), ensuring minimal impact on assay accuracy and underscoring the method's robustness and reliability.

Transitioning from direct to indirect electron transfer mechanisms, in alignment with our core principles, did not compromise our ability to analyze enzyme kinetics. Despite the complex nature of electron transfer pathways in *E. coli* (44)—which are likely more intricate than the direct transfer from the outer membrane Cyts to the periplasmic enzymes in *S. oneidensis* MR-1—the use of safranin, a highly soluble electron shuttle, enabled the observations of substrate-dependent catalytic currents. These currents conformed to the Michaelis–Menten model, as illustrated in Fig. 6. This methodological innovation broadens the potential applications of in vivo kinetic analyses, enabling the estimation of $K_m$ and $K_i$ values across a wide array of enzymes.

By exploring suitable redox mediators tailored to specific bacterial species or enzymes, we can further enhance the accuracy and versatility of electrochemical assays based on indirect electron transfer mechanisms. This approach not only broadens the applicability of our methods across various biochemical contexts but also confirms the potential of these techniques to provide detailed insights into enzymatic functions under physiological conditions. For example, in biofilms of *Pseudomonas aeruginosa*, phenazine is secreted in high concentrations. Utilizing phenazine as a redox mediator to track specific enzyme kinetics with our method could yield vital ecological insights into the roles enzymes play within biofilm contexts (45, 46).

Determining $k_{cat}$ in vivo requires accurate quantification of the total number of active enzymes participating in electrocatalysis, as this parameter normalizes reaction kinetics by enzyme abundance. In *E. coli*, where the redox mediator is uniformly distributed in the electrolyte, the total protein concentration within the reactor likely provides a reliable estimate of the active enzyme population. In contrast, in *S. oneidensis* MR-1, planktonic cells do not contribute to direct electron transfer. To address this, we carefully removed planktonic cells by washing the electrochemical reactor before the assay, ensuring a reproducible and stable electrochemical output from electrode-attached MR-1 cells (12, 17). Furthermore, *S. oneidensis* MR-1 cells are known to interact homogeneously with flat ITO electrode surfaces at the population level (47), allowing the enzyme abundance in electrode-attached cells to serve as a robust estimation of active enzyme numbers.

The integration of synthetic biology, for example, the expression of specific respiratory enzymes and MR-1 Cyts in *E. coli* (48), further broadens the scope of observable intracellular electron transfer reactions. However, the current technique may have limitations in monitoring the cytoplasmic enzyme reactions, especially those involving the $NAD^+$/NADH cycle, due to the thermodynamic challenges posed by external electrode-driven reactions (49). A promising solution lies in the synthetic biology strategy of expressing light-driven proton pumps to facilitate electron input into the cytoplasm, as evidenced in acetoin reduction reactions (49), suggesting a synergistic potential between electrochemical methods and synthetic biology to explore a wide array of intracellular respiratory enzyme kinetics.

Additionally, our research underscores the critical role of the interprotein interaction network in understanding enzymes vital for various applications, from medical drug design to biocatalysis in the food industry, energy devices, and environmental technologies (39, 50, 51). A notable application of this technique is in quantifying intracellular inhibition or inactivation by antibacterial drugs, offering a more precise assessment than traditional cell viability and growth metrics (52). This distinction is crucial for minimizing undesirable side effects by accurately identifying drug cytotoxicity versus enzyme inhibition (53). Although chemicals affecting the electron transfer pathway such as ethanol and polymyxin B have interfered with the electrochemical output, the present technique has successfully distinguished the target enzyme kinetics from other biological events, confirmed by antibiotics and inhibitors uses (Figs. 3 and 4*E* and *SI Appendix*, Figs. S6 and S7). Moreover, the high time resolution of this enzyme kinetics assay (54), coupled with the development of high-throughput systems and data-driven approaches (34, 55), presents a significant improvement over conventional substrate quantification methods,

promising a robust framework for evaluating antibacterial drugs efficiently.

In conclusion, our study introduces an electrochemical method that captures enzymatic kinetics and interprotein interactions within their cellular context. We have charted the catalytic mechanism landscape in its native environment, offering insights into enzyme function and cellular biochemistry. This breakthrough is a significant stride in unraveling the complex symphony of electron transport in cellular respiration. Our approach refines biochemical analysis, improving precision while closely reflecting physiological states, and expands our grasp of biological processes. This sets a foundation for future research to further elucidate the subtle interplay of enzymes and their networks, offering valuable insights for the broader field of biological sciences.

## Materials and Methods

**Culture Conditions of *S. oneidensis* MR-1.** *S. oneidensis* MR-1 has grown aerobically in 15 mL Luria-Bertani (LB) medium (20 g $L^{-1}$, Becton Dickinson, Sparks, MD) at 303 K for 24 h. The culture was then centrifuged at 6,000×*g* for 10 min, and the resultant cell pellet was resuspended in a 15 mL defined medium (DM; 2.5 g $L^{-1}$ $NaHCO_3$, 0.08 g $L^{-1}$ $CaCl_2$ $2H_2O$, 1.0 g $L^{-1}$ $NH_4Cl$, 0.2 g $L^{-1}$ $MgCl_2$ $6H_2O$, 10 g $L^{-1}$ NaCl, and 7.2 g $L^{-1}$ HEPES) supplemented with 0.5 g $L^{-1}$ yeast extract and 10 mM lactate. The cells were further cultivated aerobically at 303 K for 12 h. After centrifugation at 6,000×*g* for 10 min, the resultant cell pellet was washed once with DM before electrochemical measurement. Δ*fccA* and Δ*cymA* were reported by Bretschger et al. (56) and Δ*nrfA* was reported by Gao et al. (57).

**Electrochemical Measurement of *S. oneidensis* MR-1 Cells on ITO Electrodes.** Enzyme redox kinetics was monitored using a single-chamber three-electrode system (17). The reactor comprised an ITO substrate (surface area of 3.1 $cm^2$) located at the bottom of the reactor, Ag/AgCl (KCl saturated), and a platinum wire, which were used as working, reference, and counterelectrodes, respectively. Four milliliters of DM containing yeast extract (0.5 g $L^{-1}$) and lactate (10 mM) was deaerated by bubbling with $N_2$ in the reactor and then maintained at 303 K without agitation. A cell suspension of *S. oneidensis* MR-1 with an optical density at λ = 600 nm ($OD_{600}$) of 0.1 was inoculated into the reactor. The constant potential was applied at +0.40 V (vs. SHE) for 25 h using automatic polarization systems (PS-08, TOHO Technical Research Co., Ltd., Kanagawa, Japan). After confirming that *S. oneidensis* MR-1 cells are adsorbed on the ITO electrode, the supernatant in the reactor was replaced, and the ITO electrode was washed with anaerobic DM twice to remove planktonic cells as described previously (17, 58). Cathodic current from *S. oneidensis* MR-1 cells was monitored at −0.45 V vs. SHE, and CV was conducted at a scan rate of 10 $mVs^{-1}$, confirming that the scan rate is slow enough to exhibit limiting current (*SI Appendix*, Fig. S19). For the assessment of the impact of inhibitors or antibiotics, the cathodic current was monitored with 10 μM riboflavin and 5.0 mM fumarate, and the extent of relative cathodic current decreases at 10 min after the addition of antibiotics or inhibitors was also recorded. For quantification of nitrite/fumarate reduction kinetics, the cathodic currents in the absence of nitrite/fumarate were subtracted from those in the presence of nitrite/fumarate using the current at −0.80 V vs. SHE in cyclic voltammograms as the limiting currents.

**Confocal Fluorescence Microscopy.** For visualization of the cells attached to an ITO electrode ex-situ, we used a confocal laser scanning microscope (LS880, Carl Zeiss AG, Oberkochen, Germany) with a 63× water-dipping objective lens. After gently rinsing the surface of the ITO electrodes with PBS buffer, we stained the cells with SYTO 9 and propidium iodide. Finally, we obtained confocal fluorescence images of the stained cells. The excitation and emission wavelengths are 488 nm and 505 to 545 nm for SYTO 9, and 543 nm and 620 to 660 nm for propidium iodide.

**Metabolite Analysis.** 200 μL of supernatant in the electrochemical reactor was collected during constant potential application at −0.45 V (vs. SHE) in the presence of 0.1 mM nitrite or 1.0 mM fumarate and was subsequently filtered. The concentration of nitrite and fumarate in the supernatant was quantified using an ion chromatograph system (HIC-20Asuper, Shimadzu Corporation, Kyoto, Japan). Shim-pack IC-A3 (Shimadzu Corporation) was used as the column for analysis in anion chromatography kept at 40 °C with a flow rate of 1.2 mL/min. The mobile phase comprised 1.11 $gL^{-1}$ *p*-hydroxy benzoic acid, 0.67 $gL^{-1}$ Bis-Tris, and 3.09 $gL^{-1}$ boric acid. The number of electrons was calculated by subtracting the baseline cathodic current (current without nitrite/fumarate) from the cathodic current in the presence of nitrite/fumarate.

**Preparation of FccA and NrfA by Cell-Free Protein Synthesis.** FccA (NC_004347.2:c1003324-1001534) and NrfA (AE014299.2:c4117617-4116214) fused with a histidine tag at the C-terminus were expressed by the cell-free protein synthesis system, PURExfrex 2.0, (GeneFrontier, Chiba, Japan) according to the manufacturer's instructions. The template DNA sequences for cell-free protein synthesis were designed using CodHonEditor (Supplementary Data 1 and 2) to optimize codon usage to *E. coli* and synthesized by Eurofins Genomics (Tokyo, Japan). The template DNA contained the 5′-UTR (5′-GAAATTAATACGACTCACTATAGGGAGACCACAACGGTTTCCCTCTAGAAATAATTTTGTTTAACTTTAAGAAGGAGATATACCA-structure gene-3′), including the T7 promoter (underlined) and Shine–Dalgarno sequence (double underlined), and the 3′-UTR (5′-structure gene-TAATGAATAACTAATCC-3′). The template DNA was amplified by PCR using primers 5′-GAAATTAATACGACTCACTATAG-3′ and 5′-GGATTAGTTATTCATTAACCAG-3.′ Proteins were synthesized by mixing the template DNA with the PURExfrex reaction mixture at 37°C for 4 h. Synthesized proteins were purified using Ni-Sepharose 6 FF (Cytiva, Marlborough, MA). Purified protein was dialyzed against 50 mM Tris-HCl buffer (pH 8.0). To confirm the purity of the synthesized proteins, the samples were subjected to reduced SDS-PAGE (10 to 20% w/v gradient gel; ATTO Corporation, Tokyo, Japan) and stained with Rapid Stain CBB (Nacalai Tesque, Kyoto, Japan). Protein concentrations were quantified using the Micro BCA Protein Assay Kit (Thermo Fisher Scientific Inc., Waltham, MA).

**Quantification of NrfA and FccA in MR-1 Cells on ITO Electrodes.** *S. oneidensis* MR-1 cells were collected from ITO electrodes and washed using 100 mM ammonium bicarbonate buffer. The cells were then homogenized, and the proteins in the lysate were extracted with methanol and chloroform and subsequently solubilized with 8 M urea. The synthesized FccA and NrfA, along with these samples, were subjected to reductive alkylation and trypsin digestion. In the case of NrfA, the fractions corresponding to 45 to 60 kDa were extracted with SDS-PAGE before reductive alkylation and trypsin digestion (*SI Appendix*, Fig. S17). The liquid chromatography/mass spectrometry analysis was performed using a nanoadvance LC system (Bruker Daltonics, Bremen, Germany) interfaced with a Q-Exactive Plus Orbitrap mass spectrometer (Thermo Fisher Scientific Inc., Waltham, MA) via an Advance Captive Spray ionization source (AMR Inc., Tokyo, Japan), as reported previously (59). The LC process involved loading the peptides onto a trap column (L-column ODS 5 μm, Chemical Evaluation and Research Institute Japan, Tokyo, Japan) with Buffer A for concentration and desalting. The samples were then eluted from the trap column and the analytical column [Zaplous α-Pep C18 nano high-performance liquid chromatography (HPLC) column, AMR Inc., Tokyo, Japan] with a linear gradient of Buffer B from 5 to 45% at a flow rate of 500 nL $min^{-1}$ (Buffer A: 99.9% distilled water and 0.1% formic acid; Buffer B: 100% acetonitrile). The gradient time for Buffer A to B was 20 and 40 min for FccA and NrfA, respectively. The mass spectrum parameters were set as follows: electrospray voltage, 1.2 kV; temperature of the ion transfer tube, 150 °C; collision energy, 27; threshold of ion selection for MS/MS, 1700 count; mass range at 350 to 2,000 m/z, resolution at 70,000, and a maximum acquisition time of 60 ms. MS/MS scanning was performed on the top 10 abundant precursor ions with dynamic exclusion for 20 s after selection. The raw data were analyzed using Proteome Discoverer 2.4 software (Thermo Fisher Scientific Inc., Waltham, MA) with an in-house Mascotv.2.5 search engine (Matrix Science Ltd., London, UK). The following parameters were used: maximum missed cleavage sites, 2; instrument type; ESI-TRAP, precursor mass tolerance, ten ppm; fragment mass tolerance, 0.02 Da; dynamic modifications, methionine oxidation, static modification, and cysteine carbamidomethyl. All proteins were identified with a false discovery rate of <1% based on a decoy database search. The amount of NrfA and FccA in each sample was quantified by averaging the abundances of four to six peptide groups, which were quantified using LC-MS (*SI Appendix*, Table S1). A calibration curve was created for each peptide group using the synthesized NrfA and FccA, and the abundance of peptide groups contained in each sample was quantified. The average abundance of these four to six peptide groups was taken as the amount of NrfA and FccA in each sample.

**Estimation of Fumarate Reduction Rate by Supernatant Sampling.** *S. oneidensis* MR-1 cells at $OD_{600}$ of 0.2 were inoculated in a sealed bottle containing anaerobic DM with 10 mM lactate and 0 to 1.0 mM fumarate. Fumarate in the supernatant was quantified by ion chromatography before and after 10 min incubation. The fumarate consumption rate was approximated as the extent of fumarate decreased during 10 min.

**Electrochemical Measurements using a 96-Well Three-Electrode System.** *E. coli* strains BW25113 (wild type) and Δ*narG* (JW1215-KC) were cultured in LB medium. Both strains were obtained from the KEIO collection of National BioResource Project (NIG, Japan). Cells were harvested by centrifugation at 4,200×*g* for 3 min at 4 °C. The resulting pellets were resuspended in DM containing 0.5 g $L^{-1}$ yeast extract and subjected to a second centrifugation at 4,200×*g* for 3 min at 4 °C. This washing step was repeated twice. The final bacterial pellets were resuspended in DM containing 0.5 g $L^{-1}$ yeast extract, 10 mM glucose, and 20 mM nitrate, and $OD_{600}$ was adjusted to 10. Following $N_2$ gas purging for 2 h, the bacterial suspensions were again washed twice by centrifugation at 4,200×*g* for 3 min at 4 °C and resuspended in fresh DM containing 0.5 g $L^{-1}$. Electrochemical measurements were performed using a custom-made 96-well electrode plate, as previously described (34, 35). Briefly, each well is equipped with screen-printed electrodes: a carbon working electrode, a carbon counter electrode, and an Ag/AgCl reference electrode. (Fig. 6*B*). The electrodes in the wells were sterilized by UV exposure. Bacterial cell suspensions, safranin solution, and nitrate were prepared in DM containing 0.5 g $L^{-1}$ separately and mixed in the wells within an anaerobic chamber. The chamber atmosphere was maintained using a tabletop air filtration unit (KOACH T500-F, Koken, Tokyo, Japan). After sealing the plate with an aluminum cover (ALUM-1000, Diversified Biotech, Dedham, MA), it was placed in a 96-potentiostat system, originally developed at the National Institute for Materials Science, Japan (34, 35) for CV operations. CV was conducted at a scan rate of 5 mV $s^{-1}$, spanning a potential range from −1.0 V to 0 V (vs. Ag/AgCl).

**Data, Materials, and Software Availability.** The electrochemical data in 96-well three-electrode system has been deposited at Figshare (https://doi.org/10.6084/m9.figshare.28469264.v5) (60). All other data are included in the article and/or supporting information.

**ACKNOWLEDGMENTS.** We thank Prof. Dr. Nobuhiko Nomura for helpful advice. We thank Dr. Annette R. Rowe and Dr. Junki Saito for kindly providing *Shewanella oneidensis* mutant strains. *Escherichia coli* wild type and Δ*narG* (JW1215-KC) were provided from National BioResource Project (NIG, Japan). This work was financially supported by JSPS KAKENHI (20K15428, 22KK0242, 23K23532), JST ACT-X (JPMJAX211C), JST FOREST (JPMJFR231H), JST GteX (JPMJGX23B2, JPMJGX23B4), ARIM of MEXT (JPMXP1223NM5212), and the Program for Weaving Diverse Research Skills into an Orchestrated Action to Design Jubilant 100-y Lifetime Society in University of Tsukuba.

Author affiliations: [a]Department of Life and Environmental Sciences, University of Tsukuba, Tsukuba, Ibaraki 305-8572, Japan; [b]Research Center for Macromolecules and Biomaterials, National Institute for Materials Science, Tsukuba, Ibaraki 305-0047, Japan; [c]School of Life Science, Hokkaido University, Sapporo, Hokkaido 060-0808, Japan; [d]International Center for Materials Nanoarchitectonics, National Institute for Materials Science, Tsukuba, Ibaraki 305-0044, Japan; [e]School of Chemical Sciences and Engineering, Hokkaido University, Sapporo, Hokkaido 060-8628, Japan; and [f]Research Center for Autonomous Systems Materialogy, Institute of Integrated Research, Institute of Science Tokyo (Science Tokyo), Yokohama, Kanagawa 226-8503, Japan

Author contributions: Y.T. and A.O. designed research; Y.T., T.Y., and T.F. performed research; Y.T. and T.F. analyzed data; and Y.T., T.Y., T.F., and A.O. wrote the paper.

1. F. U. Hartl, M. Hayer-Hartl, Converging concepts of protein folding in vitro and in vivo. *Nat. Struct. Mol. Biol.* **16**, 574–581 (2009).
2. Y. Chen, J. Nielsen, In vitro turnover numbers do not reflect in vivo activities of yeast enzymes. *Proc. Natl. Acad. Sci. U.S.A.* **118**, e2108391118 (2021).
3. A. P. Minton, How can biochemical reactions within cells differ from those in test tubes? *J. Cell. Sci.* **119**, 2863–2869 (2006).
4. S. R. McGuffee, A. H. Elcock, Diffusion, crowding & protein stability in a dynamic molecular model of the bacterial cytoplasm. *PLoS Comput. Biol.* **6**, e1000694 (2010).
5. H. X. Zhou, G. N. Rivas, A. P. Minton, Macromolecular crowding and confinement: Biochemical, biophysical, and potential physiological consequences. *Annu. Rev. Biophys.* **37**, 375–397 (2008).
6. Y. J. Zhang *et al.*, Real-time monitoring of NDM-1 activity in live bacterial cells by isothermal titration calorimetry: A new approach to measure inhibition of antibiotic-resistant bacteria. *ACS Infect. Dis.* **4**, 1671–1678 (2018).
7. M. Lv *et al.*, Real-time monitoring of D-Ala–D-Ala dipeptidase activity of VanX in living bacteria by isothermal titration calorimetry. *Anal. Biochem.* **578**, 29–35 (2019).
8. A. Huebner *et al.*, Development of quantitative cell-based enzyme assays in microdroplets. *Anal. Chem.* **80**, 3890–3896 (2008).
9. A. Zotter, F. Bauerle, D. Dey, V. Kiss, G. Schreiber, Quantifying enzyme activity in living cells. *J. Biol. Chem.* **292**, 15838–15848 (2017).
10. R. S. Hartshorne *et al.*, Characterization of an electron conduit between bacteria and the extracellular environment. *Proc. Natl. Acad. Sci. U.S.A.* **106**, 22169–22174 (2009).
11. M. J. Edwards, G. F. White, J. N. Butt, D. J. Richardson, T. A. Clarke, The crystal structure of a biological insulated transmembrane molecular wire. *Cell* **181**, 665–673 (2020).
12. A. Okamoto, K. Hashimoto, K. H. Nealson, Flavin redox bifurcation as a mechanism for controlling the direction of electron flow during extracellular electron transfer. *Angew. Chem. Int. Ed.* **53**, 10988–10991 (2014).
13. Y. Tokunou, K. Hashimoto, A. Okamoto, Acceleration of extracellular electron transfer by alternative redox-active molecules to riboflavin for outer-membrane cytochrome c of Shewanella oneidensis MR-1. *J. Phys. Chem. C* **120**, 16168–16173 (2016).
14. D. E. Ross, J. M. Flynn, D. B. Baron, J. A. Gralnick, D. R. Bond, Towards electrosynthesis in Shewanella: Energetics of reversing the Mtr pathway for reductive metabolism. *PLoS One* **6**, e16649 (2011).
15. J. F. Heidelberg *et al.*, Genome sequence of the dissimilatory metal ion-reducing bacterium Shewanella oneidensis. *Nat. Biotechnol.* **20**, 1118–1123 (2002).
16. C. Cruz-Garcia, A. E. Murray, J. A. Klappenbach, V. Stewart, J. M. Tiedje, Respiratory nitrate ammonification by Shewanella oneidensis MR-1. *J. Bacteriol.* **189**, 656–662 (2007).
17. Y. Tokunou, K. Hashimoto, A. Okamoto, Electrochemical detection of deuterium kinetic isotope effect on extracellular electron transport in Shewanella oneidensis MR-1. *J. Visual. Exp.* **134**, 57584 (2018).
18. C. P. Cartwright *et al.*, Ethanol dissipates the proton-motive force across the plasma-membrane of Saccharomyces cerevisiae. *J. Gen. Microbiol.* **132**, 369–377 (1986).
19. E. T. Judd, M. Youngblut, A. A. Pacheco, S. J. Elliott, Direct electrochemistry of Shewanella oneidensis cytochrome c nitrite reductase: Evidence of interactions across the dimeric interface. *Biochemistry* **51**, 10175–10185 (2012).
20. C. J. Morris *et al.*, Purification and properties of a novel cytochrome: Flavocytochrome c from Shewanella putrefaciens. *Biochem. J.* **302**, 587–593 (1994).
21. S. L. Pealing *et al.*, Spectroscopic and kinetic studies of the tetraheme flavocytochrome C from Shewanella putrefaciens NCIMB400. *Biochemistry* **34**, 6153–6158 (1995).
22. C. M. Paquete, I. H. Saraiva, R. O. Louro, Redox tuning of the catalytic activity of soluble fumarate reductases from Shewanella. *Biochim. Biophys. Acta Bioener.* **1837**, 717–725 (2014).
23. A. I. Tsapin *et al.*, Identification of a small tetraheme cytochrome c and a flavocytochrome c as two of the principal soluble cytochromes c in Shewanella oneidensis strain MR-1. *Appl. Environ. Microbiol.* **67**, 3236–3244 (2001).
24. A. Donohuerolfe, G. T. Keusch, Shigella-dysenteriae-1 cyto-toxin - periplasmic protein releasable by polymyxin-B and osmotic shock. *Infect. Immun.* **39**, 270–274 (1983).
25. Y. Tokunou, K. Hashimoto, A. Okamoto, Extracellular electron transport scarcely accumulates proton motive force in Shewanella oneidensis MR-1. *Bull. Chem. Soc. Jpn.* **88**, 690–692 (2015).
26. H. Nikaido, Molecular basis of bacterial outer membrane permeability revisited. *Microbiol. Mol. Biol. Rev.* **67**, 593–656 (2003).
27. B. C. McNulty, G. B. Young, G. J. Pielak, Macromolecular crowding in the periplasm maintains α-synuclein disorder. *J. Mol. Biol.* **355**, 893–897 (2006).
28. S. J. Marritt *et al.*, The roles of CymA in support of the respiratory flexibility of Shewanella oneidensis MR-1. *Biochem. Soc. Trans.* **40**, 1217–1221 (2012).
29. D. G. G. McMillan *et al.*, Protein-protein interaction regulates the direction of catalysis and electron transfer in a redox enzyme complex. *J. Am. Chem. Soc.* **135**, 10550–10556 (2013).
30. B. M. Fonseca *et al.*, Mind the gap: Cytochrome interactions reveal electron pathways across the periplasm of Shewanella oneidensis MR-1. *Biochem. J.* **449**, 101–108 (2013).
31. C. R. Myers, J. M. Myers, Cloning and sequence of cymA a gene encoding a tetraheme cytochrome c required for reduction of iron(III), fumarate, and nitrate by Shewanella putrefaciens MR-1. *J. Bacteriol.* **179**, 1143–1152 (1997).
32. D. Leys *et al.*, Structure and mechanism of the flavocytochrome c fumarate reductase of Shewanella putrefaciens MR-1. *Nat. Struct. Biol.* **6**, 1113–1117 (1999).
33. O. Choi, B. I. Sang, Extracellular electron transfer from cathode to microbes: Application for biofuel production. *Biotechnol. Biofuels.* **9**, 11 (2016).
34. W. Miran, W. Huang, X. Long, G. Imamura, A. Okamoto, Multivariate landscapes constructed by Bayesian estimation over five hundred microbial electrochemical time profiles. *Patterns* **3**, 100610 (2022).
35. J. A. Ciemniecki, C. L. Ho, R. D. Horak, A. Okamoto, D. K. Newman, Mechanistic study of a low-power bacterial maintenance state using high-throughput electrochemistry. *Cell* **187**, 6882–6895 (2024).
36. Y. Choi, N. Kim, S. Kim, S. Jung, Dynamic behaviors of redox mediators within the hydrophobic layers as an important factor for effective microbial fuel cell operation. *Bull. Kor. Chem. Soc.* **24**, 437–440 (2003).
37. G. Rowley *et al.*, Resolving the contributions of the membrane-bound and periplasmic nitrate reductase systems to nitric oxide and nitrous oxide production in Salmonella enterica serovar Typhimurium. *Biochem. J.* **441**, 755–762 (2012).
38. J. Hirst, Mitochondrial complex I. *Annu. Rev. Biochem.* **82**, 551–575 (2013).
39. B. E. Logan *et al.*, Microbial fuel cells: Methodology and technology. *Environ. Sci. Technol.* **40**, 5181–5192 (2006).
40. J. T. Atkinson *et al.*, Real-time bioelectronic sensing of environmental contaminants. *Nature* **611**, 548–553 (2022).
41. A. Vellingiri *et al.*, Overexpression of c-type cytochrome, CymA in MR-1 for enhanced bioelectricity generation and cell growth in a microbial fuel cell. *J. Chem. Technol. Biotechnol.* **94**, 2115–2122 (2019).

42. S. J. Marritt *et al.*, A functional description of CymA, an electron-transfer hub supporting anaerobic respiratory flexibility in Shewanella. *Biochem. J.* **444**, 465–474 (2012).
43. B. Schuetz, M. Schicklberger, J. Kuermann, A. M. Spormann, J. Gescher, Periplasmic electron transfer via the c-type cytochromes MtrA and FccA of Shewanella oneidensis MR-1. *Appl. Environ. Microbiol.* **75**, 7789–7796 (2009).
44. L. E. Doyle, E. Marsili, Weak electricigens: A new avenue for bioelectrochemical research. *Bioresource. Technol.* **258**, 354–364 (2018).
45. N. R. Glasser, B. X. Wang, J. A. Hoy, D. K. Newman, The pyruvate and alpha-ketoglutarate dehydrogenase complexes of Pseudomonas aeruginosa catalyze pyocyanin and phenazine-1-carboxylic acid reduction via the subunit dihydrolipoamide dehydrogenase. *J. Biol. Chem.* **292**, 5593–5607 (2017).
46. J. A. Ciemniecki, D. K. Newman, NADH dehydrogenases are the predominant phenazine reductases in the electron transport chain of Pseudomonas aeruginosa. *Mol. Microbiol.* **119**, 560–573 (2023).
47. S. Pirbadian, M. S. Chavez, M. Y. El-Naggar, Spatiotemporal mapping of bacterial membrane potential responses to extracellular electron transfer. *Proc. Natl. Acad. Sci. U.S.A.* **117**, 20171–20179 (2020).
48. A. Anand *et al.*, Laboratory evolution of synthetic electron transport system variants reveals a larger metabolic respiratory system and its plasticity. *Nat. Commun.* **13**, 3682 (2022).
49. N. M. Tefft, M. A. TerAvest, Reversing an extracellular electron transfer pathway for electrode driven acetoin reduction. *ACS Synth. Biol.* **8**, 1590–1600 (2019).
50. M. B. Pedersen, P. Gaudu, D. Lechardeur, M. A. Petit, A. Gruss, Aerobic respiration metabolism in lactic acid bacteria and uses in biotechnology. *Annu. Rev. Food Sci. Technol.* **3**, 37–58 (2012).
51. M. A. Lobritz *et al.*, Antibiotic efficacy is linked to bacterial cellular respiration. *Proc. Natl. Acad. Sci. U.S.A.* **112**, 8173–8180 (2015).
52. J. W. Mouton *et al.*, MIC-based dose adjustment: Facts and fables. *J. Antimicrob. Chemoth.* **73**, 564–568 (2018).
53. K. D. Greis *et al.*, Development and validation of a whole-cell inhibition assay for bacterial methionine aminopeptidase by surface-enhanced laser desorption ionization-time of flight mass spectrometry. *Antimicrob. Agents Chemother.* **49**, 3428–3434 (2005).
54. C. Leger, P. Bertrand, Direct electrochemistry of redox enzymes as a tool for mechanistic studies. *Chem. Rev.* **108**, 2379–2438 (2008).
55. M. Tahernia *et al.*, A 96-well high-throughput, rapid-screening platform of extracellular electron transfer in microbial fuel cells. *Biosens. Bioelectron.* **162**, 112259 (2020).
56. O. Bretschger *et al.*, Current production and metal oxide reduction by Shewanella oneidensis MR-1 wild type and mutants. *Appl. Environ. Microbiol.* **73**, 7003–7012 (2007).
57. H. C. Gao *et al.*, Reduction of nitrate in Shewanella oneidensis depends on atypical NAP and NRF systems with NapB as a preferred electron transport protein from CymA to NapA. *ISME J.* **3**, 966–976 (2009).
58. A. Okamoto, Y. Tokunou, K. Shafeer, K. Hashimoto, Proton transport in the outer-membrane flavocytochrome complex limits the rate of extracellular electron transport. *Angew. Chem. Int. Ed.* **56**, 9082–9086 (2017).
59. Y. Yabe *et al.*, Comparative proteome analysis of the ligamentum flavum of patients with lumbar spinal canal stenosis. *JOR Spine.* **5**, e1210 (2022).
60. T. Fujikawa, Electrochemical measurement of *E. coli*. Figshare. https://doi.org/10.6084/m9.figshare.28469264.v5. Accessed 27 February 2025.